



ELSEVIER

Journal of Magnetism and Magnetic Materials 190 (1998) 332–348

M Journal of
M magnetism
M and
magnetic
materials

Magnetic states of small cubic particles with uniaxial anisotropy

W. Rave^{a,*}, K. Fabian^b, A. Hubert^c^a*Institut für Metallische Werkstoffe, IFW Dresden, Helmholtzstr. 20, D-01069 Dresden, Germany*^b*FB Geowissenschaften, Universität Bremen, Postf. 330440, D-28334 Bremen, Germany*^c*Institut für Werkstoffwissenschaften der Universität Erlangen-Nürnberg, Martensstr. 7, D-91058 Erlangen, Germany*

Received 3 August 1998

Abstract

The lowest energy states in small cubic particles with uniaxial anisotropy are explored as a function of anisotropy strength and particle size. The investigations result in a phase diagram which contains the boundaries between the regions of one, two and three domains (flower, vortex and double vortex states). While the general features of the phase diagram are derived from energy estimates based on domain theory, the details are obtained using numerical micromagnetics. The two-domain and the three-domain phase can be subdivided into subphases. The comparison between different configurations revealed that a twisted vortex configuration with an S-shaped domain wall replaces the symmetric vortex with a straight wall at larger sizes. The three-domain phase contains two subphases which are symmetric with respect to (1 0 0) and (1 1 0) mirror planes, respectively. The transition from two to three domains occurs into the (1 1 0)-three-domain-state (diagonal state). This structure can be described as a configuration with two (quarter-) circular domain walls in two opposing corners. However, this configuration is energetically favored only in a small region within the phase diagram relative to the (1 0 0)-symmetry three-domain state with straight walls (sandwich state). © 1998 Published by Elsevier Science B.V. All rights reserved.

PACS: 75.60; 75.40.Mg

Keywords: Small particles; Magnetic domains; Micromagnetic simulations

1. Introduction

The lowest-energy state of a magnetic particle depends on its size, its shape, and the strength and character of its anisotropy. In order to get an overview over a well-defined case we focus on a cubic

particle in zero field. The magnetic anisotropy of the particle is assumed to be uniaxial, with the easy axis along one of the cubic axes. Employing reduced variables (see Section 2 for details) we are left with two dimensionless parameters: the relative anisotropy $Q = K_u/K_d$ with K_u being the uniaxial anisotropy constant and $K_d = J_s^2/(2\mu_0)$, and the reduced length $\lambda = L/\sqrt{A/K_d}$ where L is the particle size and A is the exchange stiffness constant.

* Corresponding author. + 49-351-465-9531; fax: + 49-351-465-9537; e-mail: w.rave@ifw-dresden.de.

In the following the easy axis of the uniaxial anisotropy is taken to coincide with the z -axis of the cube (see Fig. 1). This is exactly the case which was first explored by Schabes and Bertram [1], who calculated numerically the equilibrium configurations for small anisotropy and relatively small particles. The question of the equilibrium configurations in the full range of relative anisotropies and for larger particles – extending the size into the multidomain range – was first addressed in Section 3.3.5 of Ref. [2], in search for a justification of domain patterns in general.

First results as well as domain-theoretical estimates were offered there. Here the full range of equilibrium patterns is analyzed, reaching in the anisotropy spectrum from $Q = 0$, over very soft ($Q \ll 1$) and intermediate ($0.1 < Q < 1$) to hard magnetic materials ($Q > 1$), and in size up to 100 times the exchange length $\sqrt{A/K_d}$.

For small λ ($\lambda < 5$) it is well known that a more or less uniformly magnetized state prevails. This also remains true for magnetic cubes where in spite of the logarithmic divergence of the stray field at the edges and corners, the angular variation of the magnetization due to this divergence is confined to a volume [3] extending about one exchange length $\sqrt{A/K_d}$ from the corner, largely independent of Q .¹ Being magnetized basically along the easy axis (we will call this the ‘longitudinal’ orientation), the *single domain* or *flower state* carries only little anisotropy energy. Also the exchange stiffness energy is small because the magnetization pattern is fairly uniform. The predominant energy term in the single domain state is the stray field energy which will be somewhat smaller than $\frac{1}{3}K_d$, the demagnetizing energy density of the uniformly magnetized cube (which is the same as that of a sphere).

With increasing sample size, inhomogeneous states become energetically favorable: for small and intermediate Q this is the *curling* or *vortex state* [1]. This closed-flux configuration avoids most of the stray field energy at the expense of a large exchange stiffness energy. If the vortex axis is oriented perpendicular to the anisotropy axis, this ‘transverse’

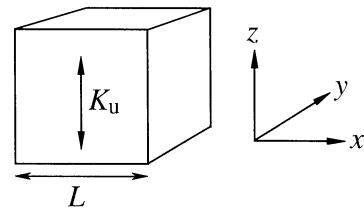


Fig. 1. Sketch of the cube and coordinates.

vortex state also saves some anisotropy energy, but this is of minor importance for small Q . No continuous transition between the longitudinal single domain state and the transverse vortex state is conceivable. Instead, we observe a discontinuous phase boundary which defines the *single-domain limit* between both states. Because the exchange stiffness energy density of the vortex state scales with A/L^2 , the single domain limit scales for small Q with the exchange length $\sqrt{A/K_d}$ and is thereby largely independent of K_u .

Of particular interest is the transition between the vortex configuration for intermediate sizes, and regular domain patterns to be expected for larger particles and in bulk material. Here we identify this *multidomain limit* – somewhat arbitrarily – with the equilibrium transition between the vortex and a three-domain state. For small Q both the vortex state and the *three-domain* or double vortex states will be largely stray-field-free. The only reason for the formation of a flux-closed three-domain state is, that it saves anisotropy energy at the expense of exchange stiffness energy. Therefore the particle size at the second phase transition will scale with the classical wall width parameter $\sqrt{A/K_u}$, thus increasing in units of the exchange length $\sqrt{A/K_d}$ with decreasing Q .

Samples with dimensions between the two limits are predicted to display continuous micromagnetic patterns which differ from the classical domain picture. In Section 3.3 of Ref. [2], arguments are presented for the occurrence of similar continuously varying zones of this size below the surface of strongly misoriented bulk crystals. The calculated phase diagram of micromagnetic states in small particles can therefore serve as a guide to the character of domain structures also in extended samples

¹ An extension of this work from 2D to 3D was demonstrated by a recent analytical micromagnetic treatment [4].

which certainly cannot be treated with rigorous micromagnetic methods.

These and similar arguments are discussed in a more systematic way in Section 2 using the framework of domain theory to derive the general features of the phase diagram of micromagnetic states in cube-shaped particles. The quantitative exploration uses the tools of numerical micromagnetics which are introduced in Section 3. The following sections on results start with a classification of the possible magnetic configurations in cubes (Section 4.1) followed by a comparison of simple vortex states close to the single domain limit in Section 4.2, the twisted or asymmetrical vortex observed at larger particle size (Section 4.3), and the three-domain states at the multidomain limit (Section 4.4).

The lowest energy solutions lead to a phase diagram of the primary configurations which is established in Section 5. Finally the stability limit of the vortex state is analyzed in Section 6. There also the special case $Q = 0$ will be discussed, explaining why the single domain limit is difficult to calculate for small Q .

2. General energy estimates

Here the general features of the phase diagram are derived by means of domain-theoretical energy estimates. This is done separately for the two limiting cases of very low and high anisotropy.

2.1. Low Q materials

The total micromagnetic energy for a fixed configuration in a magnetically uniaxial cube-shaped particle of size L can be expressed as

$$E_{\text{tot}} = K_u \varepsilon_k L^3 + K_d \varepsilon_d L^3 + A \varepsilon_x L. \quad (1)$$

Here the dimensionless coefficients ε_k , ε_d and ε_x depend only on the chosen configuration. For example, a cube magnetized uniformly along the easy axis has $\varepsilon_d = \frac{1}{3}$ and $\varepsilon_k = \varepsilon_x = 0$. In this way the energy of one configuration can be extended to particles of different size L or anisotropy K_u . If there are arguments that the same configuration

will also be approximately valid for different parameter sets, we can transfer the results of one calculation to related cases. Introducing reduced quantities according to

$$\varepsilon_{\text{tot}} = E_{\text{tot}}/(K_d L^3), \quad \lambda = L/\sqrt{A/K_d}, \quad Q = K_u/K_d \quad (2)$$

leads to

$$\varepsilon_{\text{tot}} = \varepsilon_k Q + \varepsilon_d + \varepsilon_x/\lambda^2. \quad (3)$$

To derive the phase boundary between two fixed configurations I and II for which the assumed approximate independence on λ and Q is valid, Eq. (3) is used for both:

$$\varepsilon_{\text{tot}}^{\text{I}} = \varepsilon_k^{\text{I}} Q + \varepsilon_d^{\text{I}} + \varepsilon_x^{\text{I}}/\lambda^2, \quad \varepsilon_{\text{tot}}^{\text{II}} = \varepsilon_k^{\text{II}} Q + \varepsilon_d^{\text{II}} + \varepsilon_x^{\text{II}}/\lambda^2. \quad (4)$$

The equal-energy thickness (phase boundary) is given by

$$\lambda_{\text{pb}} = \sqrt{\frac{\varepsilon_x^{\text{II}} - \varepsilon_x^{\text{I}}}{\varepsilon_d^{\text{I}} - \varepsilon_d^{\text{II}} + (\varepsilon_k^{\text{I}} - \varepsilon_k^{\text{II}})Q}}. \quad (5)$$

For the single domain (I) – vortex (II) transition which will occur at a small particle size λ , the demagnetizing energy ε_d and the exchange energy contributions ε_x are predominant as mentioned in the introduction. Therefore $\varepsilon_d^{\text{I}} - \varepsilon_d^{\text{II}}$ will be dominant in the denominator, and the phase boundary of the single-domain-vortex transition will become independent of Q for small Q .

At the second phase boundary (= multidomain limit) from the vortex (I) to the three-domain state (II) which we anticipate at a large reduced size λ , the demagnetizing energies ε_d^{I} and $\varepsilon_d^{\text{II}}$ will be negligible for both states, the more so the larger the reduced size λ . The second term in the denominator of Eq. (5) will be decisive even when Q approaches zero, leading to a phase boundary $\lambda_{\text{pb}2}$ which increases with $1/\sqrt{Q}$ for decreasing Q . For detailed predictions the formation of domain walls has to be taken into account. A simple Landau–Lifshitz-type domain model avoids stray field energies completely and again predicts a $1/\sqrt{Q}$ -dependence of $\lambda_{\text{pb}2}$. Estimates based on a refined domain model (p. 328 of Ref. [2]) yield $\lambda_{\text{pb}2} \simeq 25/\sqrt{Q}$, or explicitly $L_{\text{pb}2} \simeq 25\sqrt{A/K_d}/\sqrt{Q} = 25\sqrt{A/K_u}$ for the multidomain limit. The same generalized domain theory

predicts $\lambda_{pb1} \simeq 7$ or $L_{pb1} \simeq 7\sqrt{A/K_d}$ for the single-domain limit at small Q .

2.2. High Q materials

In the other extreme, $Q \gg 1$, exchange and anisotropy energies will be concentrated in *domain walls*. The vortex state is transformed in this limit into a classical two-domain state [5], and the double-vortex state is converted into a three-domain state. In every micromagnetic model both the exchange energy and the anisotropy energy will therefore scale with the classical Bloch wall energy parameter $\sqrt{AK_u}$, so that the total energy can be expressed as

$$E_{tot} = \sqrt{AK_u}\eta_k L^2 + K_d \varepsilon_d L^3 + \sqrt{AK_u}\eta_x L^2, \quad (6)$$

where $\eta_k = \varepsilon_k \lambda \sqrt{Q}$ and $\eta_x = \varepsilon_x / (\lambda \sqrt{Q})$ are effective domain wall areas of a model. In reduced form (using the definitions in Eq. (2)) the total energy becomes

$$\varepsilon_{tot} = \varepsilon_d + (\eta_k + \eta_x) \sqrt{Q} / \lambda. \quad (7)$$

Analogous to the previous case, the phase boundary λ_{pb} between two different models is found from the equilibrium condition at

$$\lambda_{pb} = \frac{\eta_k^I - \eta_k^{II} + \eta_x^I - \eta_x^{II}}{\varepsilon_d^{II} - \varepsilon_d^I} \sqrt{Q}. \quad (8)$$

For large Q , η_k and η_x will be about equal, as in classical domain walls. Both phase boundaries, that between the single-domain state and the two-domain state as well as that between the two-domain and the three-domain state, therefore increase with \sqrt{Q} in the chosen reduced units when Q increases. Inserting the definition of the reduced length λ from Eq. (2) we see that in this parameter range the phase boundaries scale with $\sqrt{AK_u/K_d}$.

By evaluating the stray-field coefficients for the simple domain structures (sketched in Fig. 14) quantitative estimates for the phase boundaries are obtained. The single domain limit for high anisotropy becomes: $\lambda_{pb1} = 25\sqrt{Q}$ or $L_{pb1} = 25\sqrt{A/K_u}Q$.

Similarly the multidomain limit can be derived from domain theoretical calculations. In p. 164 of Ref. [2], a transition between the simple two-do-

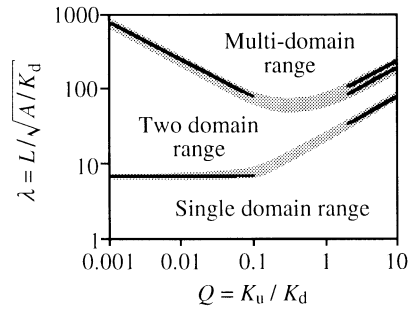


Fig. 2. Sketch of the phase diagram as based on domain theory alone, using the asymptotic behavior for large and small Q derived in this section. The regions where the exact phase boundaries are anticipated are indicated by the gray shaded areas.

main state and a ‘diagonal’ three-domain state (consisting of a main domain and two quarter-circular domains, for a sketch see Fig. 14e) was found at $\lambda_{pb2} = 60.8\sqrt{Q}$. A second transition to a sandwich three-domain state (three domains separated by straight walls along a $[1\ 0\ 0]$ -direction) was found at $\lambda_{pb2} = 76\sqrt{Q}$.

Altogether, a phase diagram as sketched in Fig. 2 is expected. The connections between the asymptotic lines at small and large Q cannot be calculated reliably with domain-theoretical arguments and need rigorous numerical micromagnetic calculations. Conversely, numerical methods cannot reach the very large sizes at the multidomain limit for large and for small Q , so that the final phase diagram which will be presented in Fig. 15 must lean on domain-theoretical arguments in these parts.

3. Micromagnetic techniques

The numerical calculations in this paper have been obtained by two independently developed programs. It was therefore possible to compare the results and check for hidden programming errors. Both programs minimize the sum of exchange, anisotropy and stray-field energy discretized with a periodic grid. Throughout the paper we only present equilibrium states which were reached when the effective field was at every mesh point in the configuration smaller than a certain ε (typically

chosen as 10^{-3} times the anisotropy field H_k). The first code is based on a 3D extension of methods previously applied to two dimensions [3,6]. The second program goes back to the 3D code of Ref. [7]. It was later improved [8] incorporating ideas developed in Refs. [9,10]. Cube-shaped particles with the material parameters of the mineral *magnetite* have been analyzed with this program line already in Refs. [7,8]. After establishing the equivalence of the results for our problems, the more demanding tasks were performed with the first algorithm which is therefore explained in more detail.

Both codes calculate the stray-field energy using cubic cells for which analytic expressions for the self and interaction energies both of volume and surface charges are available (p. 122f of Ref. [2] or Refs. [8,9,11]). With these expressions the scalar potential at every point of the discretization grid can be expressed as a convolution of the chosen charges with the fixed interaction expressions. Once the potential is known, the stray field is obtained by a gradient operation, and the stray field energy results from multiplying potential and charge at every point and summing over this product. An effective field of which the stray field is an important part is used in our modified steepest descent and relaxation (MDSR) algorithm [10,12]. The total energy alone is used in this algorithm in the interleaved energy minimization steps.

The convolution was performed in Fourier space [6,13]. By using charges and the scalar potential instead of magnetization and field vectors, only Fourier transformations on these scalar quantities are necessary, a forward transformation of the charges, and a backward transformation of the potential. If only the total energy is needed, this can be calculated directly in Fourier space [8], leaving only one necessary Fourier transformation.

In addition, the efficiency was increased by taking into account the fact that only real numbers have to be transformed because both charges and interaction coefficients are real. The transformation of rows which consist of zeros only (this occurs necessarily due to the zero-padding operation) are omitted. This was possible because also higher-dimensional FFTs were performed based on one-dimensional FFT routines [14].

Because the interaction coefficients are even functions (not depending on the sign of the coordinate differences between two cells) the Fourier transforms of the interaction functions are real and less multiplications in frequency space are needed than in the general complex case. Finally, FFT operations which are necessary for different potential contributions can be combined due to the linearity of the Fourier transform operation. For example, the potential contributions in volume cells due to volume charges are calculated in frequency space. After an inverse FFT in the z -direction, the potential contribution due to xy -charge sheets are added. The remaining inverse FFTs along the x - and y -directions are then performed together.

A further advantage of the employed FFT routines is the option to use with good efficiency not only powers of two in each dimension for the number N of cells, but also other integers containing factors of three or five. Thus, we could fill the gap between $N = 32$ and $N = 64$ cells along one dimension with efficient calculations using $N = 36, 40, 48, 50, 54,$ and 60 cells. We were able to use a maximum of 128^3 (about 2 million) cells in our micromagnetic calculations performed on Hewlett Packard 9000 workstations.

The feature of a larger flexibility of the lattice density is very important because finite element calculations can generally only be considered valid if they prove to be independent of the degree of discretization. An extrapolation to infinite N is necessary for reliable results, and as the computation time even in efficient algorithms increases at least with N^6 (N^3 because of the stray field, another N^3 for the energy minimization), the possibility to use smaller increments is of great practical importance. Fig. 3 shows an example of the chosen procedure to calculate the equal energy point of two configurations, the longitudinal flower and the transverse symmetric vortex state in this case. The energy of the flower state remains almost independent of the reduced cube size λ , while the vortex energy decreases roughly with $1/\lambda^2$ as predicted by Eq. (5). The intersection is calculated numerically by interpolation for different lattices as shown in (a). The resulting values for the single domain limit are then plotted in (b) as a function of the number

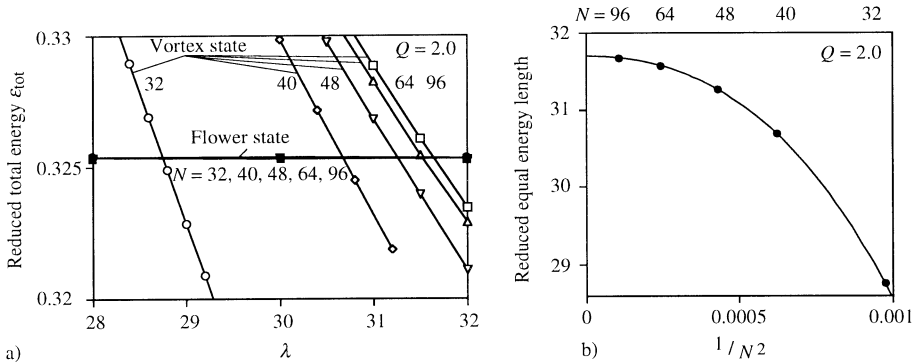


Fig. 3. Calculating a configurational phase boundary and extrapolating the result to an infinitely fine mesh. In (a) the energies of the flower and the simplest vortex state (see Fig. 5) are plotted as a function of the reduced cube size λ for different numbers of cells in one dimension N . The intersection points are then plotted in (b) as a function of $1/N^2$, allowing an extrapolation towards an infinitely fine mesh.

of cells N . Using $1/N^2$ as the abscissa, an extrapolation towards $1/N^2 = 0$ can be convincingly achieved.

As in earlier two-dimensional studies [3,15] the necessary degree of discretization was found to be about two cells per exchange length for small Q . For large Q the wall width parameter $\sqrt{A/K_u}$ becomes smaller than the exchange length $\sqrt{A/K_d}$ so that an even finer discretization is necessary. Usually, we started each calculation with a test function for a certain configuration evaluated on a moderate mesh, and minimized the total energy for this discretization. Then the number of cells was increased and the old solution is interpolated on the new grid to serve as the new starting function. Sometimes solutions with a reduced symmetry or the proper configuration of domain walls and other features develop only at a higher discretization level due to discretization grid pinning effects at insufficient discretization. The best way to obtain the data needed in extrapolations was therefore to go back from the finest mesh to coarser meshes. This time the interpolated fine-mesh solution is used as the starting function for the coarsened meshes.

4. Classification and prototype solutions

Even though we constrain ourselves to the basically simple case of cubic particle shape and

uniaxial anisotropy with the axis parallel to a cube edge, there exists a surprising variety of stable and metastable micromagnetic configurations. Topological properties (such as the number and character of magnetization vortices) allow to group the possible configurations as will be discussed in the following section. We focus on stable solutions, discussing the even greater manifold of metastable configurations primarily on a qualitative level.

4.1. Swirls, edge and corner configurations

The number of metastable solutions increases especially at small Q where the pole-avoidance principle assumes priority. A configuration with a small stray-field energy corresponds to a unit vector field which is divergence-free in the volume and which lies approximately parallel to the surface everywhere. This is not perfectly possible for topological reasons. At least two surface vortices or ‘swirls’ [16] must exist somewhere on the surface. In the center of these swirls or quasi-singularities the magnetization either points into the body of the cube, or away from it. If more than two swirls are present, some of them must have a negative revolution number (‘cross-vortices’) so that the weighted sum of all swirls is again two as required by Poincaré’s theorem [17].

In a certain class of solutions for small Q and intermediate size every edge will be almost uniformly magnetized in one of the two directions

parallel to itself. For the twelve edges of a cube there are thus 4096 possible configurations. In the case of zero anisotropy each of these belongs to one of 76 classes, the members of which are equivalent with respect to cubic symmetry. By taking into account uniaxial anisotropy the number of equivalence classes increases to 186. However, if some of the mentioned swirls are allowed to be located on an edge, the number of essentially different solutions becomes still larger.

Another aspect is the magnetization configuration in the corners. Here two possible alternatives exist depending on the orientation of the magnetization on the adjacent edges [16]: either all three of them are oriented towards or away from the corner (*tripod* configuration) which forces the magnetic moment directly in the corner to point along a radial axis, or one edge is oriented differently from the others (*saddle* corner; see the sketches in Fig. 4). The tripod always represents a swirl with a positive revolution number, the saddle configuration is not singular in the topological sense.

In larger particles the number and arrangement of *domain walls* turn out to play the dominant role in classifying the different configurations. The point and line structures (the corner types, surface swirls, and the vortex cores connecting the swirls) only lead to a subdivision of the main categories which are given by the number of domains.

4.2. Simple vortices near the single-domain limit

The vortex structure can be recognized as the configuration with the minimum number of swirls on the surface, replacing the flower state above the single domain limit. Examples for vortex solutions slightly above the single-domain limit are presented in Fig. 5. The Q -values were chosen as $Q = 0.002$, 0.3 and 4 representative for some soft magnetic elements, and hexagonal Co and NdFeB single crystal particles, respectively. The reduced sizes are $\lambda = 10$, 15 and 40. For the case $Q = 0.3$ the 3D view of the particle surface is supported by a cross section at the central z -position. While for $Q = 4$ a two-domain state essentially consisting of two antiparallel flower states is found, a semi-hard material (Co) already shows a magnetization component parallel to the edges induced by the stray field.

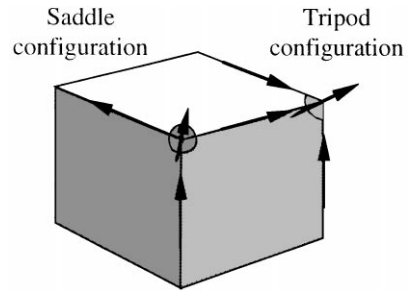


Fig. 4. The two possible configurations in a corner: (a) Tripod, for which all three edge magnetizations either converge towards the corner or diverge from it. (b) Saddle, with one converging and two diverging edge magnetizations, or vice versa.

For the soft element a fully developed curling pattern is observed. The interior wall which can clearly be discerned in the two-domain state for $Q = 4$ widens to fill the particle, leading to a typical vortex for $Q = 0.002$.

4.3. Vortices in larger particles

All stable vortices in larger particles have an axis in a plane perpendicular to the anisotropy axis, and in their core the magnetization lies by definition parallel to the vortex axis which we choose as the y -axis. For small sizes – near the single domain limit – the magnetization on the y -edges is aligned at least partially along the magnetization in the vortex axis. This is due to the exchange interaction which is most effective for small particles. When the cube size increases the ‘flower opens’, i.e. the magnetization on these edges rotates away from the parallel orientation. For high anisotropy it turns towards a direction more or less parallel to the anisotropy axis, becoming perpendicular to the vortex core. For low anisotropy the magnetization on the y -edges turns backward, thus reaching an effectively demagnetized state. All these transitions occur continuously with increasing particle size as shown in Fig. 6. Thus, there exists no phase transition between ‘parallel’ vortices and ‘antiparallel’ vortices.

However, even though the y -edge magnetization progressively rotates into its energetically most favorable orientation with increasing size, other

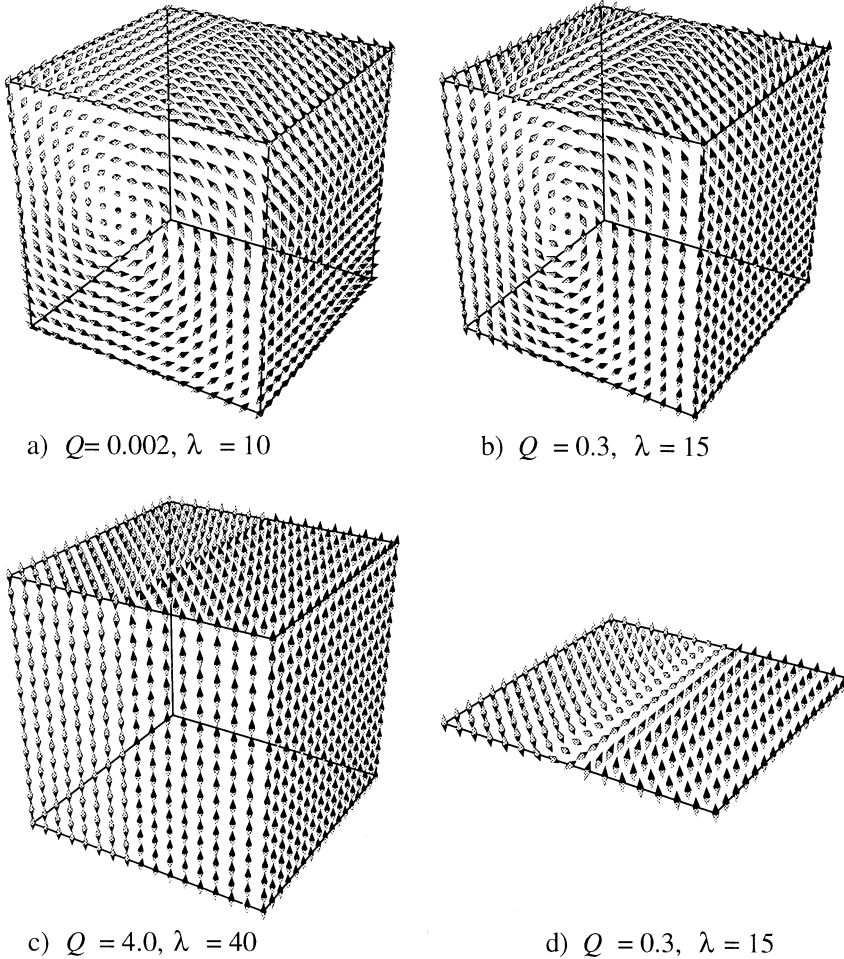


Fig. 5. Small vortices close to the single domain-vortex transition. In addition, a cross section of the central xy -plane for the solution (b) shows the straight wall in the interior.

alignments relative to the vortex core become possible in larger particles. Altogether seven different possibilities exist for the relative orientation of m_y on the four y -edges and the vortex core. A parameter pair for which all seven configurations were found to be at least metastable² is $Q = 0.1$ and

²Stability or metastability could be proved rigorously by showing that the matrix of second derivatives of the energy with respect to the magnetization components is positively definite. In practice, this is not feasible and we only determined that the matrix of first derivatives (the ‘effective field’ perpendicular to the magnetization) was zero everywhere. The fact that there really exist small energy barriers between the configurations seems rather probable, however, because we reached the config-

$\lambda = 40$. We visualize the configurations by central xz -cross sections (lying perpendicular to the vortex axis, which is oriented along the y -direction) in Fig. 7. Grayscale maps depict the m_y -component. In black regions the magnetization points out of this plane, while in white regions it points into it.

urations using Ritz functions for the starting states where the magnetization was changed appropriately on the y -edges. The fact that the energy landscape in configuration space guided these configurations to the desired states indicates the existence of the local minima. A finer mesh or a more stringent relaxation criterion did not change the results either.

Intermediate grey levels indicate an in-plane magnetization. In addition the reduced total energies are indicated. For this parameter set the demagnetized state (g) has the lowest energy, while the state

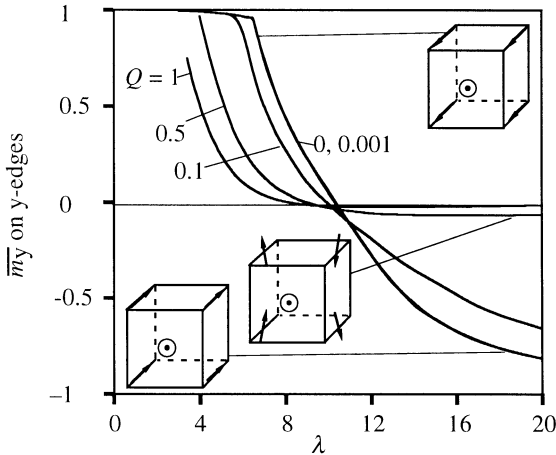


Fig. 6. The averaged edge magnetization component m_y of vortex states, demonstrating the continuous deviation from an alignment of the edges parallel to the vortex core at small sizes. For small Q and large size a demagnetized state with negative edge magnetization is favored. For large Q and large size the edges turn parallel to the easy axes, leading to a vanishing y -component.

with the smallest exchange energy (a) has the highest total energy.

There exists even another modification of the vortex structure which was not foreseen by the topological arguments presented so far. Characteristic for this variant is a twist in the structure connected with an S-shaped bending of the wall. It turned out that for large sizes this modification can save more demagnetizing energy than it costs exchange or wall energy. It thus becomes the lowest energy state in a certain part of the phase diagram. We termed this configuration the *twisted vortex*. Its character is visualized in Fig. 8, where the faces and the cross section of the central xy -plane are shown for the parameters $Q = 0.01$ and $\lambda = 70$. While for moderate and large Q only a slight bending is found, it becomes more distinct for small Q and increasing size.

The transition between the twisted and the lowest-energy symmetrical vortex was investigated for $Q = 0.1$ as a function of particle size. As a measure for the twisting or asymmetry we took the difference in the net flux in the z -direction on the back and front xz -surfaces. From Fig. 9a follows that the twisted vortex becomes favorable above $\lambda = 43.5$ for the chosen Q value, where a first order transition between the straight and the

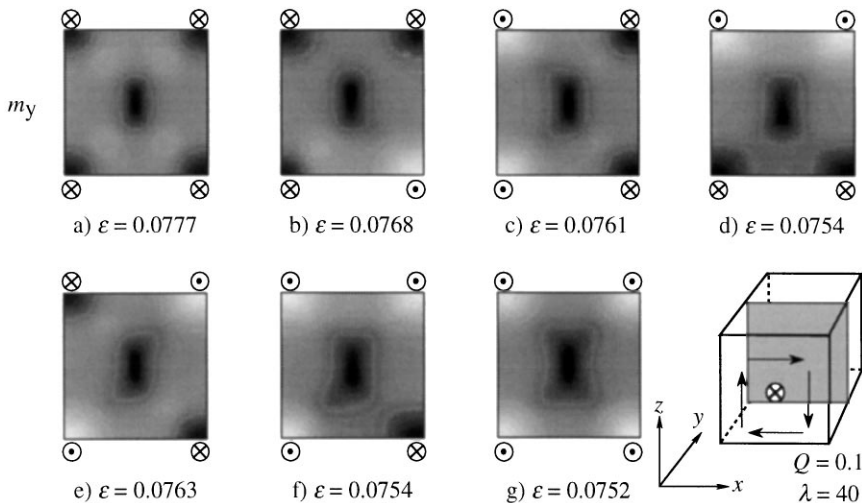


Fig. 7. Vortices in larger particles for $Q = 0.1$ and $\lambda = 40$. The magnetization component m_y in the cross section of the central xz -plane is represented in grayscale, indicating the relative orientation of the magnetization in the vortex core and the y -edges. In addition, the reduced total energies of the configurations are indicated.

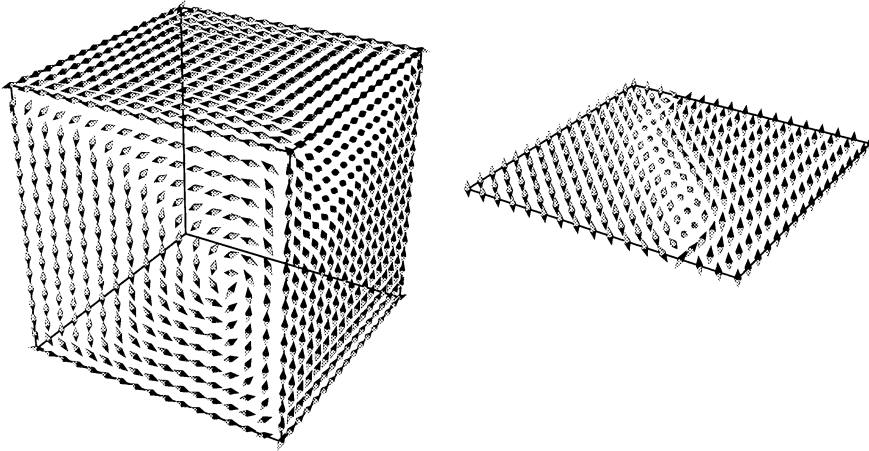


Fig. 8. Side faces and central xy -plane of the twisted vortex for $Q = 0.01$ and $\lambda = 70$.

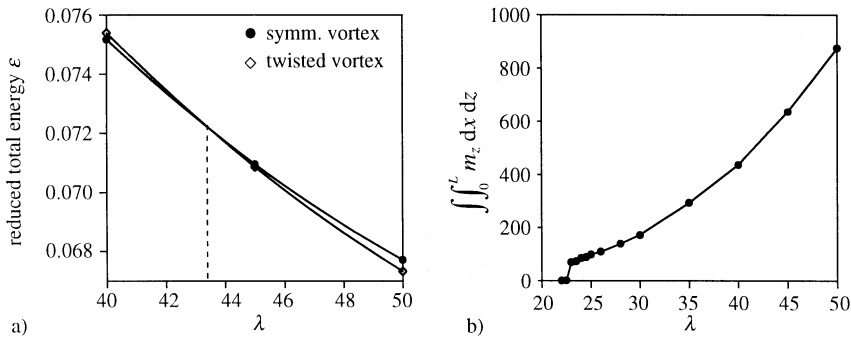


Fig. 9. The transition between the twisted vortex and the symmetrical vortex of lowest energy for $Q = 0.1$. In (a) the energies of twisted and simple vortex solutions are compared, showing a first order phase transition at $\lambda = 43.5$ beyond which the twisted vortex solution becomes absolutely stable. In (b) the stability of the twisted vortex is tested by plotting a measure of the asymmetry of the configuration as a function of particle size. The twisted vortex turns out to be metastable in a large size range until it becomes unstable below about $\lambda = 22$.

twisted vortex occurs. With decreasing size the twisted vortex remains metastable with decreasing twisting amplitude as shown in Fig. 9b. It can be followed down to about $\lambda = 22$ where the configuration collapses into a straight transverse vortex.

4.4. Three-domain states at the multi-domain limit

While none of the possible magnetization structures with four surface swirls proved to be stable in our tests, there are two distinct stable states with six quasi-singularities on the surfaces of the cube. Two

basic classes of such states were identified as stable solutions. In the first class each of the six cube faces contains one swirl. This leads to a diagonal three-domain state with quarter-circular walls. In the other class two vortices are packed next to each other on two opposing surfaces, balanced by two cross vortices in the middle of two edges.

Both structures are presented in Figs. 10 and 11 with views of their side faces and central cross sections of the xy -planes, respectively. The latter aspect gives a clear view of the internal wall and domain arrangement. Both structures can be

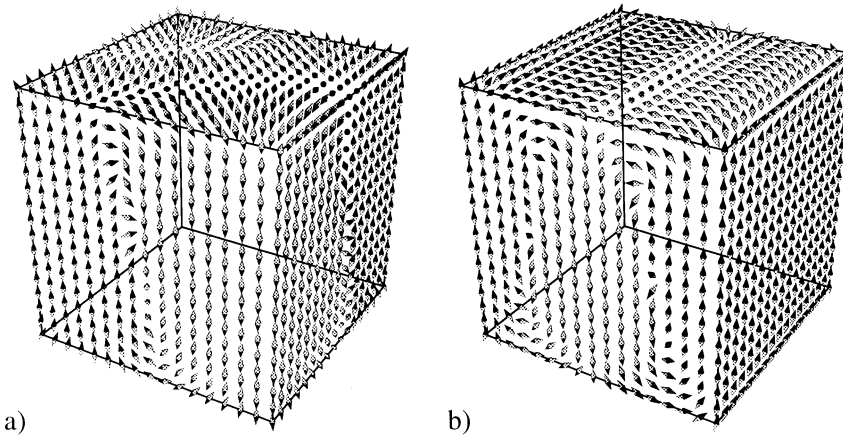


Fig. 10. Three-domain states with walls along the $[1\ 1\ 0]$ -direction (a) and along a $[1\ 0\ 0]$ -direction (b) for $Q = 0.5$ and $\lambda = 55$.

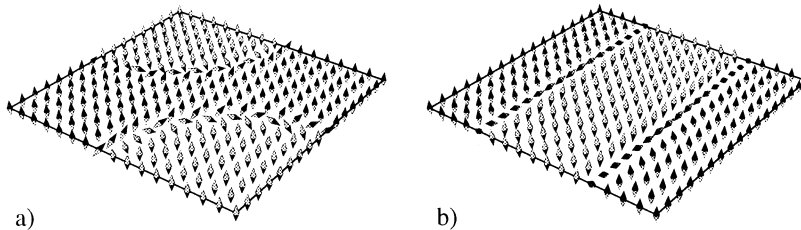


Fig. 11. Cross sections through the central xy -plane of (a) the diagonal and (b) the sandwich three-domain structures shown in Fig. 10.

recognized as three-domain states which may also be understood as $[1\ 1\ 0]$ - and $[1\ 0\ 0]$ -double vortices, respectively.

As in the case of single-vortex configurations, there are several modifications of the double-vortex states which differ in the relative orientation of vortex cores and vortex-parallel edges. Due to the less demanding discretization requirements we chose a size of $\lambda = 40$ for this example (compared to Fig. 10, this affects the magnetization angles only marginally). The $(1\ 0\ 0)$ -oriented double vortex which represents a simple sandwich-type three-domain state shows lowest energies if the flux produced by the vortex cores is closed by an antiparallel orientation of the magnetization vectors on the parallel edges (see Fig. 12c and Fig. 12d for a comparison of the xz -cross sections of two different solutions). For the $(1\ 1\ 0)$ -double vortex configurations the orientation of the magnetization in the

swirl centers turned out to be important. Previously, the structure of Fig. 12b was found as a metastable state [8] resulting from a configurational transition out of the single domain state as the cube size was increased. Trying out several modifications, we found that an energetically favorable structure (a) is formed when neighboring swirls on the side surfaces have opposite polarity (one pointing into the cube, one pointing out of it). The reason is seen in the gray-scale maps of the m_x - and m_y -components in the central xy -plane (Fig. 12a and Fig. 12b). With this polarity of the swirls the flux can be transported easily along the walls. For the chosen size in Fig. 12 the diagonal state with curved walls (a) is energetically favored compared to the sandwich state (c). The same relation was found also for other Q -values, and it extends up to the multidomain limit at which three-domain states become absolutely stable (see phase diagram in

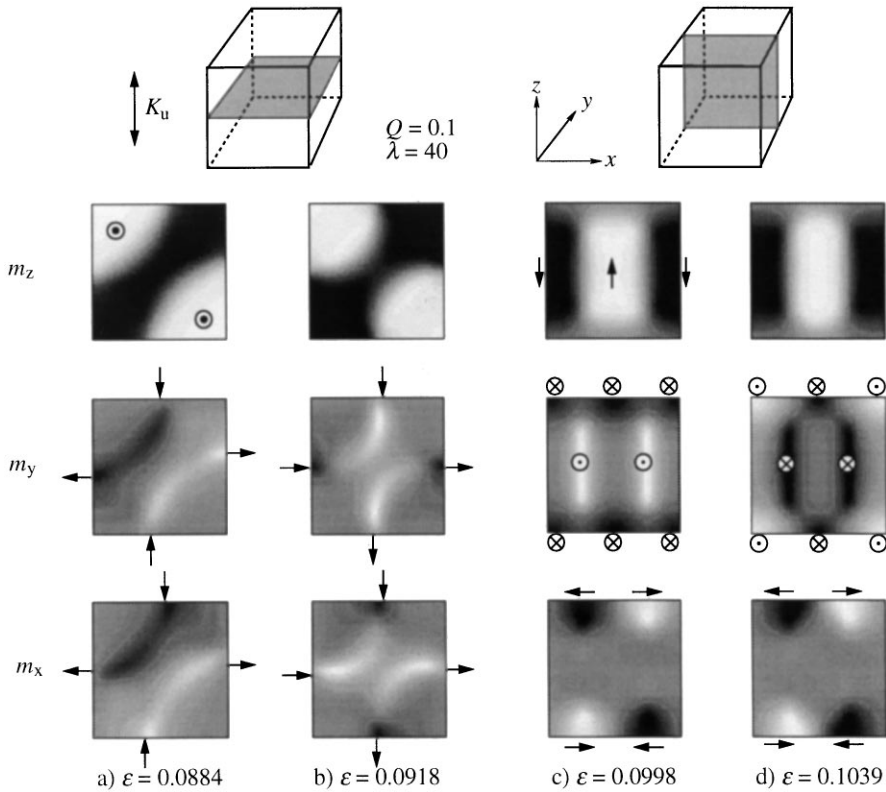


Fig. 12. Cross sections for the magnetization components m_x , m_y and m_z through modifications of the different three-domain states. (a, b) shows the central xy -plane of the diagonal three-domain states with different orientation of the core magnetization. Configuration (a) is slightly favored due to its simpler internal wall magnetization pattern. The sandwich state can be understood better by plotting the magnetization components in the central xz -cross section. Parameters in all cases are $Q = 0.1$ and $\lambda = 40$. Configuration (c) in which the m_y -component (middle row) is effectively closed is energetically favored over (d).

Section 5). This energy difference, however, is small, and at cube sizes slightly above the phase boundary the energy difference is offset by a gain in stray-field energy, making the sandwich structure the lowest energy minimum. An example for the energetic transitions from two to three domains is shown for the case $Q = 0.5$ in Fig. 13. Here four different structures become close in energy: the symmetrical and the twisted vortex as well as the two types of three-domain states. At this Q -value the twisted vortex cannot compete. We find a phase boundary at $\lambda = 55.1$ from the simple vortex to the $[1\ 1\ 0]$ three-domain state, and at $\lambda = 62.4$ another transition to the sandwich state.

Summarizing our search for the lowest energy states, we found five ground-state configurations

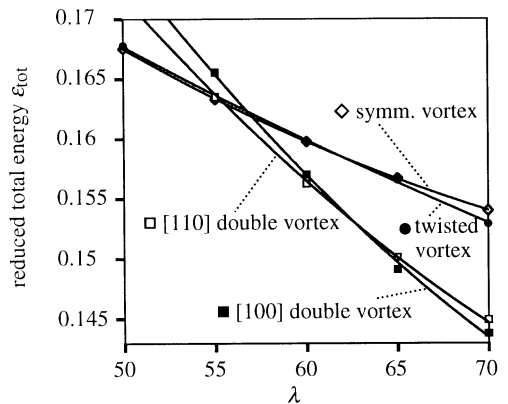


Fig. 13. Energies near the multidomain limit which lies for $Q = 0.5$ at $\lambda = 55.1$. An additional transition from the diagonal to the sandwich three-domain structure occurs at $\lambda = 62.4$.

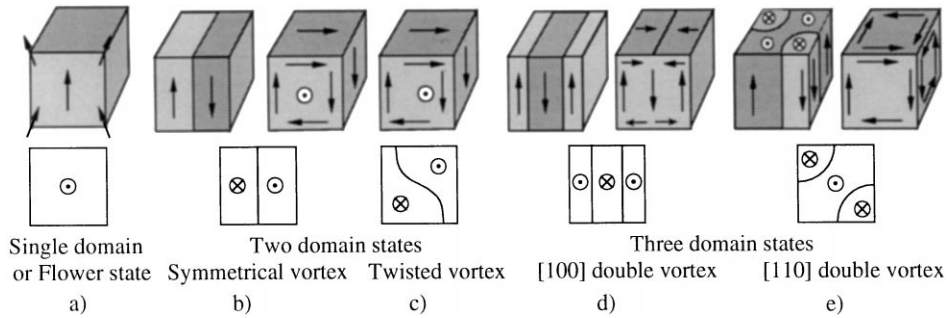


Fig. 14. The energetically favored one, two and three-domain states: (a) flower state, (b, c) two-domain states for high and low anisotropy, (d, e) three-domain states for high and low anisotropy. The sketches in the second row always show the central slice in the z -direction indicating the walls and domains.

which are shown schematically in Fig. 14. In three cases we show the same basic configuration in a low- Q and in a high- Q variant. These variants differ strongly in their outward appearance (top row), but little in their internal, cross sectional aspect (bottom row).

5. Phase diagram of cube-shaped magnetic particles

The phase diagram of Fig. 15 was obtained by equating the energies of the different configurations, and extrapolating the intersection points to infinite discretization. In the two-domain phase region a boundary indicates the stability range of the twisted vortex structure. In the same way the phase boundary between the diagonal and the sandwich three-domain states is indicated within the three-domain phase region. Only configurations with a reduced size smaller than $\lambda = 80$ could be reliably calculated numerically. To extend the phase boundaries to larger sizes the data were extrapolated according to the estimates presented in Section 2. To allow for a more precise comparison with other results we present two tables with values of the phase boundary points (Table 1), and the associated energies and magnetization values for a selection of the phase boundary points (Table 2).

Previously published values for the first phase boundary in uniaxial cube-shaped particles can be found in [1] (with the correction reported in [18]) where a single domain limit of $\lambda = 6.8$ for $Q = 0.02$ was found, in comparison to our result of $\lambda = 7.28$.

These older results, and also those reported in [19] for small Q are roughly compatible with our values, taking into account that they were not extrapolated to infinitely fine discretization (see Fig. 3). Previous calculations for large values of Q are obviously unreliable: a value of $12.4\sqrt{A/K_d}$ was obtained for $Q = 1.3$ in [19], instead of $24.1\sqrt{A/K_d}$ according to our calculations. This discrepancy must be attributed to insufficient discretization in the older calculations which leads to a severe underestimation of the exchange energy.

Also of interest is the comparison of results for uniaxial spheres obtained by Aharoni and Jakubovics. For the single-domain radius they found $R = 10.65\sqrt{A/K_d}$ for $Q = 0.338$ (Co) [20] which has to be compared with our results for cubes of $L = 11.58\sqrt{A/K_d}$. One may assume as a guideline that the single-domain limit is roughly independent of shape, depending primarily on volume. Under this assumption a single-domain radius of $R = 7.19\sqrt{A/K_d}$ for the cobalt sphere would be expected based on our results which still lies above the rigorous lower bound derived for fine ferromagnetic particles [21]. The actually calculated larger value [20] must be ascribed to the fact that Aharoni and Jakubovics calculated rotationally symmetric states only. The transverse vortex which is clearly the energetically favored low-magnetization state because it can save anisotropy energy does not belong to this class.

The phase transition at $Q = 0.1$ from the single-domain state to the symmetrical vortex state

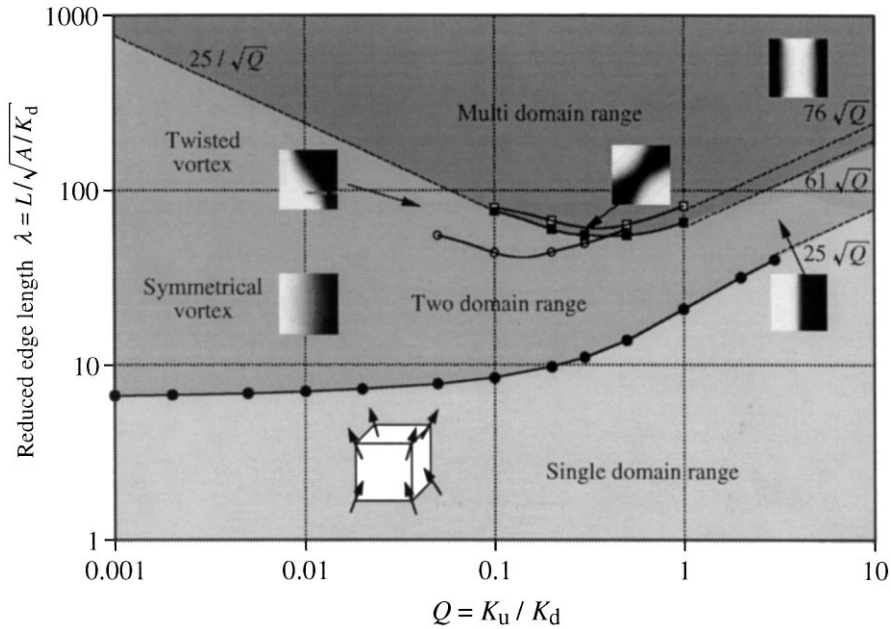


Fig. 15. Phase diagram of zero-field states of cubic-shaped particles with uniaxial anisotropy. The inserted icons represent the m_z -components in a xy -cross section, thus revealing the basic domain pattern of the various configurations.

Table 1
Extrapolated points of the first and second phase boundary

Q	10^{-3}	10^{-2}	0.1	0.2	0.3	0.5	1.0	2.0	3.0
λ_{pb1}	6.66	7.04	8.47	9.76	11.03	13.82	20.88	31.72	40.03
λ_{pb2}	–	–	75.7	59.6	55.2	55.1	65.4	–	–

was proposed as a benchmark problem for micromagnetic calculations [22]. The detailed extrapolated values for the partial energies and the average magnetization components along the three axes for this phase boundary point can be found in Table 2.

In a recent submission to Ref. [22] Hertel and Kronmüller discovered that a further configuration interacts with the single-domain limit as calculated in this paper. At slightly lower thicknesses a longitudinal vortex is formed continuously out of the flower state. For the chosen example of $Q = 0.1$ this happens at $\lambda_{crit} = 8.2$ according to our own calculations with which we reproduced and confirmed the configuration found by Hertel and Kronmüller.

This has to be compared to our previous single domain limit at $\lambda = 8.47$ (see Table 1). Obviously, an initial gain in stray-field energy can already be achieved when the symmetrical longitudinal flower state starts to decay into a longitudinal vortex. Only at a larger size (at $\lambda = 8.50$ in the case of $Q = 0.1$) the longitudinal vortex is replaced by the transverse vortex that has a lower anisotropy energy in uniaxial particles.

For low Q the phase boundary for the ‘single-domain limit’ in Fig. 15 thus must be replaced by a double boundary: (i) a continuous, second-order transition between the flower state and a longitudinal vortex state, (ii) a discontinuous switching transition between the longitudinal and a transverse

Table 2

Energies and magnetization values of selected points on the phase boundaries. The upper part belongs to the single-domain limit, the lower part to the multidomain limit. The abbreviations are f for flower state, sv for symmetrical vortex, tv for twisted vortex and dv for the [1 1 0]-double vortex (diagonal state). Again all values are extrapolated to an infinitely fine mesh

Q	λ	ε_{tot}	ε_{d}	ε_{x}	ε_{k}	m_{x}	m_{y}	m_{z}	conf.
10^{-3}	6.66	0.3071	0.2867	0.0203	0.0000	0.000	0.000	0.978	f
			0.2509	0.0551	0.0009	0.000	0.905	0.000	sv
0.1	8.47	0.3027	0.2794	0.0177	0.0056	0.000	0.000	0.971	f
			0.0783	0.1723	0.0521	0.000	0.352	0.000	sv
1.0	20.88	0.3187	0.3052	0.0010	0.0125	0.000	0.000	0.994	f
			0.1047	0.0921	0.1241	0.000	0.070	0.038	sv
2.0	31.72	0.3253	0.3176	0.0002	0.0075	0.000	0.000	0.998	f
			0.1349	0.0843	0.1062	0.000	0.043	0.016	sv
0.1	75.7	0.0567	0.0068	0.0104	0.0394	-0.008	0.014	0.000	tv
			0.0055	0.0176	0.0335	-0.018	-0.018	-0.012	dv
1.0	65.4	0.1991	0.1149	0.0271	0.0571	0.000	0.025	0.010	sv
			0.0757	0.0497	0.0741	-0.032	-0.032	-0.050	dv

vortex. The splitting of this phase boundary occurs at $Q = 0.12$. For stronger anisotropy an onset of curling appears only at sizes beyond the single-domain limit.

An important consequence of this finding is that the flower state cannot remain metastable beyond the single-domain limit in low- Q cube-shaped particles, because it will spontaneously decay into the longitudinal vortex state. The nature of the continuous flower–vortex transition for the transverse orientation will be discussed in the following section.

6. Stability limit of the vortex state in small particles

For small Q the single-domain limit comes very close to the size at which the (transverse) vortex state collapses into a transverse flower state, a state with a high average magnetization perpendicular to the easy axis. This collapse at the stability threshold between the vortex state and the flower state represents a second order phase transition for which the symmetry is reduced from mirror (flower state)

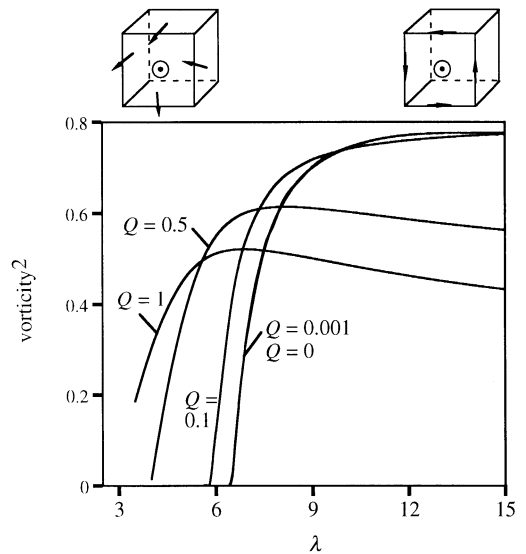


Fig. 16. The suppression of the vortex state at small particle size is studied for different Q -values by plotting the integral vorticity as a function of size. For small Q it vanishes at a critical size, marking a second-order phase transition to a transverse flower state. This transition is not reached for larger Q (shown here for the example of $Q = 1$) where the already weak vortex becomes unstable with respect to a conversion to a standard, longitudinal flower state.

to chiral symmetry (vortex state). It can be monitored by measuring the *integral vorticity* of the vortex which we define as the line integral of the circumferential magnetization on a plane orthogonal to the vortex axis (Fig. 16).

The energy of the transverse flower state is larger than the energy of the longitudinal flower state by an amount of the order of the anisotropy parameter Q . This makes the determination of the intersection point of the energy curves more difficult for smaller anisotropy. In the limit $Q = 0$ no conventional, first-order single-domain limit is expected to exist at all. It coincides with the phase transition of the

transverse vortex state to the transverse flower state, the latter being energetically equivalent to the longitudinal flower state for zero Q . For all other values the single domain limit is given by a first order phase transition at which both longitudinal and transverse states are stable, separated by a threshold. The vanishing of the threshold leading to a continuous transition between the energy curves of flower and vortex states in the case $Q = 0$ is shown in Fig. 17. The equivalence of the stability limit with the phase boundary in this special case can be used to derive the single-domain limit for the case $Q = 0$ as well. Extrapolating the square of the integral vorticity to zero we derived $\lambda_{pb1} = 6.49$.

Additionally, we looked at flower and vortex states with $[1\ 1\ 1]$ -orientation in order to find out whether a reorientation of the axis could save exchange energy at small sizes and for low Q . As can also be seen in Fig. 17 the $[1\ 1\ 1]$ -flower state is even for zero anisotropy for all sizes energetically less favorable than its $[1\ 0\ 0]$ counterpart. The $[1\ 1\ 1]$ -vortex gets around 7.8 length units very close to its $[1\ 0\ 0]$ version, but even there the $[1\ 1\ 1]$ vortex is not favored. If $[1\ 1\ 1]$ -oriented states play no role as stable solutions even for zero anisotropy, this is not expected to be different for finite uniaxial anisotropy with an $[0\ 0\ 1]$ easy axis in contrast to the negative cubic anisotropy case studied in [8]. $[1\ 1\ 1]$ -oriented states can be obtained as metastable solutions. Visualizations of these states which confirm that they were correctly reached are shown in Fig. 18.

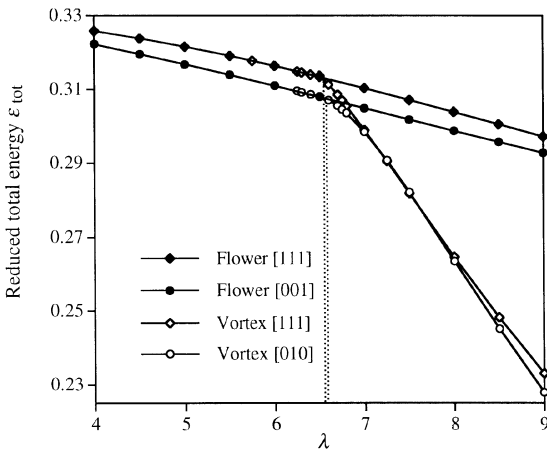


Fig. 17. The second order phase transition from the vortex to the flower state for $Q = 0$ for two different orientations.

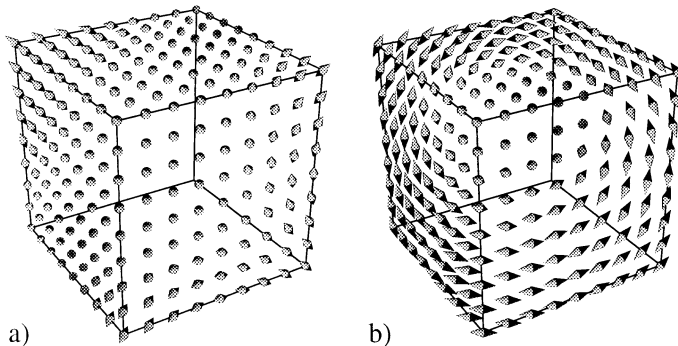


Fig. 18. The metastable flower (a) and vortex (b) states oriented along the $[1\ 1\ 1]$ -direction for $Q = 0$ and $\lambda = 7.5$ seen from the $[1\ 1\ 1]$ -direction.

7. Conclusions and outlook

We systematically collected the magnetic equilibrium states of lowest energy in cube-shaped magnetic particles. Subtle phenomena for which more complicated computations become necessary are the twisted vortex pattern and the precise geometry of the most favorable three-domain states which we established for the first time. Summarizing the results of the micromagnetic calculations one notes that most of the main features of the phase diagram can already be obtained with a good understanding of domains, while on the other hand only by comparison with the exact calculations a feeling for the limits of domain theory is gained. In addition, the stability limit of vortices for small sizes was calculated and the nature of the single domain limit for the case of vanishing anisotropy was clarified.

The extension of this work to different aspect ratios, the calculation of the magnetization curve and switching fields, as well as the search for more metastable states are possible and may be addressed in future work. For geophysics the investigation of octahedral particles with negative anisotropy constant would be of interest.

Acknowledgements

Major parts of this work were orally presented at Joint MMM-Intermag Conference, San Francisco 1998 as well as on the Spring Meeting of the Deutsche Physikalische Gesellschaft at Regensburg. Support by a grant of VW-Stiftung is gratefully acknowledged by W.R. Thanks for helping to develop the display routine in Mathematica are due to Sean Geoghegan.

References

- [1] M.E. Schabes, H.N. Bertram, *J. Appl. Phys.* 64 (1988) 1347.
- [2] A. Hubert, R. Schäfer, *Magnetic Domains – The Analysis of Magnetic Microstructures*, Springer, Berlin, 1998.
- [3] W. Rave, K. Ramstöck, A. Hubert, *J. Magn. Magn. Mater.* 183 (1998) 328.
- [4] A. Thiaville, D. Tomáš, J. Miltat, *Phys. Stat. Sol. (b)*, submitted.
- [5] C. Kittel, *Phys. Rev.* 70 (1946) 965.
- [6] D.V. Berkov, K. Ramstöck, A. Hubert, *Phys. Stat. Sol. (a)* 137 (1993) 207.
- [7] W. Williams, D.J. Dunlop, *Nature* 337 (1989) 634.
- [8] K. Fabian, A. Kirchner, W. Williams, F. Heider, T. Leibl, A. Hubert, *Geophys. J. Int.* 124 (1996) 89.
- [9] K. Ramstöck, T. Leibl, A. Hubert, *J. Magn. Magn. Mater.* 135 (1994) 97.
- [10] D.V. Berkov, K. Ramstöck, T. Leibl, A. Hubert, *IEEE Trans. Magn.* 29 (1993) 2548.
- [11] M.E. Schabes, A. Aharoni, *IEEE Trans. Magn.* 23 (1987) 3882.
- [12] K. Ramstöck, *Mikromagnetische Rechnungen an isolierten und eingebetteten Strukturen*, Dissertation, Univ. Erlangen, 1997, pp. 19–29.
- [13] S.W. Yuan, H.N. Bertram, *IEEE Trans. Magn.* 28 (1992) 2031.
- [14] K. Ramstöck, P. Lockey, Convolution package based on the Netlib FFT package by P. Schwarztrauber (available from <ftp://magnet.www.uni-erlangen.de/MAGFEM>).
- [15] W. Rave, A. Hubert, *J. Magn. Magn. Mater.* 184 (1998) 179.
- [16] A. Hubert, *J. Phys. (Coll.)* 49 (C8) (1989) 1859.
- [17] M. Kléman, *Points, Lines and Walls*, Vol. I, Wiley, Chichester, 1983.
- [18] M.E. Schabes, *J. Magn. Magn. Mater.* 95 (1991) 249.
- [19] N.A. Usov, S.E. Peschany, *J. Magn. Magn. Mater.* 110 (1992) L1.
- [20] A. Aharoni, J.P. Jakubovics, *Phil. Mag. B* 53 (1986) 133.
- [21] W.F. Brown, *J. Appl. Phys.* 39 (1968) 993.
- [22] R.D. McMichael, *Micromagnetic Standard Problem #3*, <http://www.ctcms.nist.gov/~rdm/mumag.html>: μ Mag – Micromagnetic Modeling Activity Group, 1998.